University of Glasgow

MacLaren, I. et al. (2020) A comparison of a direct electron detector and a high-speed video camera for a scanning precession electron diffraction phase and orientation mapping. Microscopy and Microanalysis, 26(6), pp. 1110-1116.

http://eprints.gla.ac.uk/227096/

Deposited on: 7 January 2021

A comparison of a direct electron detector and a high speed video camera for scanning precession electron diffraction phase and orientation mapping

Ian MacLaren[1], Enrique Frutos-Myro[2], Damien McGrouther[1], Sam McFadzean[1],

JK Weiss[3], Doug Cosart[3], Joaquim Portillo[4,5], Alan Robins[4], Stavros Nicolopoulos[4]

Eduardo Nebot del Busto[6] and Richard Skogeby[6]

1 School of Physics and Astronomy, University of Glasgow, Glasgow G12 8QQ
2 School of Engineering, University of Glasgow, Glasgow G12 8QQ
3 NanoMEGAS USA, 1095 W Rio Salado Parkway, Suite 110, Tempe, Arizona 85281, USA
4 NanoMEGAS SPRL, Bd.Edmond Machtens 79 bte 22, 1080 BRUSSELS, Belgium
5 Centres Cientifics i Tecnologics, Universitat de Barcelona, Sole i Sabaris, 1 - 3, 08028 Barcelona, Catalunya
6 Quantum Detectors Ltd., R104, RAL, Harwell, Oxford OX11 0QX, UK

ABSTRACT

A scanning precession electron diffraction system has been integrated with a direct electron detector to allow the collection of improved quality diffraction patterns. This has been used on a 2-phase α-β titanium alloy (Timetal® 575) for phase and orientation mapping using an existing pattern-matching algorithm and has been compared to the commonly-used detector system, which consisted of a high speed video camera imaging the small phosphor focusing screen. Noise is appreciably lower with the direct electron detector, and this is especially noticeable further from the diffraction pattern center where the real electron scattering is reduced and both diffraction spots and inelastic scattering between spots are weaker. The results for orientation mapping are a significant improvement in phase and orientation indexing reliability, especially of fine nanoscale laths of a-Ti, where the weak diffracted signal is rather lost in the noise for the optically coupled camera. This was done at a dose of ~19e⁻Å⁻², and there is clearly a prospect for reducing the current further whilst still producing indexable patterns. This opens the way for precession diffraction phase and orientation mapping of radiation sensitive crystalline materials.

INTRODUCTION

Precession electron diffraction started life as a promising way to produce pseudo-kinematical diffraction patterns (Vincent & Midgley, 1994), which allows an easier interpretation of diffracted intensities (Gjønnes, 1997) and thereby quantitative crystallography in the transmission electron microscope (Gjønnes, et al., 1998; Mugnaioli, et al., 2009). Initially, this was simply an improved method of generating patterns to record onto photographic film, whereby using a small precession angle (often < 1°) increases the reliability of structure solutions (Vincent & Midgley, 1994). The dynamic range of film is high, and this recording method is ideal for single diffraction patterns. But, it was later realized that precession electron diffraction could become a key part of automated techniques like scanning precession electron diffraction (SPED) for orientation mapping (Rauch, et al., 2010) or automated diffraction tomography (Kolb, et al., 2007; Mugnaioli, et al., 2009). This requires, however, that the diffraction patterns are recorded electronically. Specifically, for the orientation mapping, this is challenging, as just with EBSD, large areas

can only be mapped with high spatial resolution with a relatively fast camera. Most CCD cameras used in electron microscopy until recently were simply not fast enough for the purpose – early ones were only capable of 1-2 frames per second, and even more recent ones only get to about 30 frames per second. For this reason, (Rauch, et al., 2010) used a different approach of using a small high-speed video-rate CCD for imaging the small fluorescent focus screen in the microscope, which could go faster than 100 frames per second. Of course, this solution is somewhat limited by a few issues, including the response time of the phosphor on the screen, the indirect and noisy results of the excitation of the phosphor and the blurring of the diffraction pattern on this, and the further noise and blurring introduced by the high speed CCD camera. Nevertheless, this provides an excellent method for determining maps of crystal phase and orientation using a pattern matching algorithm.

Recent advances in electron microscopy have centered around the development of new pixelated direct electron detectors, i.e. those in which detection does not depend on conversion to light in a phosphor, followed by the detection of the photons. Most of these detectors work on the principle of directly creating electron-hole pairs in a semiconductor, which are then collected and read out in some way. These detectors can be roughly split into two groups. Firstly, there are radiation-hardened monolithic CMOS detectors that have large numbers of pixels (16, 24 or even 64 megapixel cameras are available from different manufacturers) and are well suited for high resolution imaging in transmission electron microscopy mode, and have been key to the recent revolution in structural biology (Ramachandra, et al., 2014; Ruskin, et al., 2013). These detectors, although capable of withstanding direct exposure to high-energy electrons, will generally suffer damage from the high intensity spots in electron diffraction patterns. For this reason, a second type of detector using a so-called hybrid pixel sensor is used for recording high-intensity electron intensity distributions, but at a much lower pixel count than the monolithic sensors (128×128 or 256×256 pixels are common) (Beacham, et al., 2011; Mac Raighne, et al., 2011; Mir, et al., 2017; Ryll, et al., 2016; Tate, et al., 2016; Yang, et al., 2015a). These are particularly useful as detectors for the diffraction pattern in the back focal plane in scanned electron beam techniques (Krajnak, et al., 2016; Tate, et al., 2016; Yang, et al., 2015a; Yang, et al., 2017), as many of the diffractive imaging modes do not need an exceptionally high number of pixels (e.g. ptychography (Pennycook, et al., 2015; Yang, et al., 2015b)). Moreover, fast readout at a few milliseconds per pixel or better makes such detectors suitable for use in a range of scanned diffraction imaging modes, including differential phase contrast (Krajnak, et al., 2016) and HOLZ-STEM (Nord, et al., 2019a). Specifically, one of the key advantages of some of these detectors is that they count individual electron events and consequently have no readout or amplifier noise in the counts, provided the threshold for counting is set correctly. This means that the detective quantum efficiency (DQE) can be exceptionally high, limited mainly by the spreading of the primary beam electrons in the sensor. At low primary beam energies, the size of the resulting electron hole pair generation region on the detector is lessened and high DQE and extended modulation transfer function (MTF) have been demonstrated at 60 and 80kV for the Medipix by (Mir, et al., 2017).

It has already been demonstrated that scanned nanobeam electron diffraction using direct electron detectors gives high quality, low noise data suitable for analysing crystallography with nanometre resolution (Doherty, et al., 2020; Johnstone, et al., 2020b). It is therefore high time that SPED benefits from these advances in detectors in order to be

able to reduce the noise and improve the pattern definition, while operating at readout speeds even higher than those of video cameras. This article reports the integration of one such pixelated direct detection system (Merlin for EM) with a scanning precession electron diffraction (SPED) system, together with a systematic test of this system. Specifically, the test is performed of mapping similar areas of a two-phase nanostructured alloy using both the direct electron detector and the standard Stingray camera, and then comparing the results by analysing the resulting datasets using a well-known pattern matching algorithm (Rauch, et al., 2010) to perform phase and orientation mapping. This provides a useful test case which will be familiar to many users of precession electron diffraction systems. It is expected that the lower noise would result in improved template matching and fewer false positives from intrinsically weak and noisy patterns and that the improved definition would result in improved accuracy of distinction between similar diffraction patterns from different orientations or different phases. Thus, the direct comparison of the results from the same area using the two detectors should provide a good test as to whether using direct electron detection provides significant advantages for SPED in one common application of this technique. It should be noted that this is just one way to process and use SPED data, and that recent work in scanned nanobeam electron diffraction and SPED has increasingly used open source libraries to process the data in a number of ways (Doherty, et al., 2020; Johnstone, et al., 2020a; Johnstone, et al., 2020b; Martineau, et al., 2019; Sunde, et al., 2019), and that the advantages being investigated in this work would also provide advantages to such methods.

EXPERIMENTAL

Precession electron diffraction was performed using NanoMEGAS Digistar hardware interfaced with a JEOL ARM200cF (scanning) transmission electron microscope (STEM). The microscope was operated at 200kV in conventional TEM mode (TEM-L setting) with the smallest spot size, spot 5, and the smallest (10μm) condenser aperture. This gives a low beam current and a small convergence angle for the spot of 0.3mrad. Data was collected using 100Hz precession at a precession angle of 1° and 10ms per pixel. Two datasets were acquired from the same area of the same sample to provide a direct comparison. The first dataset was recorded using the standard NanoMEGAS video camera (Stingray), which works by imaging the small fluorescent focusing screen in the microscope. This allows recording up to 580x580 pixel images, although the detector is most commonly used in the software for scanning precession electron diffraction and orientation mapping reading out either 288x288 or 144x144 (binned) pixel; in the current experiment, the latter 144x144 mode at 8-bit dynamic range was used to maximize signal to noise, seeing as pixel resolution was not considered to be critical for template matching (when each diffraction spot spreads across several pixels). The second dataset was recorded using a Quantum Detectors Merlin for EM direct electron detector, a system based on the 256x256 pixel Medipix-3 chip bump bonded to a 500μm thick Silicon sensor and a custom high speed (>1kHz) read out system, and the detector was installed on a retractable mount in the wide-angle port of the microscope. The Merlin readout was set to work in 12-bit mode, which means that the counter on each pixel can count up to 4096 hits. This number could be exceeded in 10ms with a bright beam, seeing as the detector can count individual hits up to about 1MHz. Seeing as the beam current used in the experiment was low when using a small spot size, small camera length and short exposure time, dynamic range was not going to be a problem in either case. At higher beam currents, saturation could be a problem and the Stingray camera

would clearly saturate sooner, but this was not tested in this work. The data from both cameras was acquired using NanoMEGAS Topspin software, which also synchronously controlled the Digistar hardware for precession and beam deflection in order to produce SPED datasets.

To test the performance of the two different detectors, a dual-phase Ti alloy, Timetal ® 575 was used. This sample was prepared using a conventional FIB liftout procedure using a FEI Helios Plasma FIB (Thermo Fisher Scientific Inc.) using Xe ions for the milling. The area chosen for the analysis was an area at the edge of a large primary α grain, at which there is a region of β containing coarser secondary α laths and very fine tertiary α laths. This provided an excellent test as it contained everything from large, single-grain, single-phase regions, to fine nanostructures with laths just a few tens of nm wide.

The data was treated in two ways. Firstly, single patterns were exported from two equivalent positions in the scans, one on a secondary alpha lath, and one in a region that appeared likely to be mostly beta. These were analysed to compare noise levels and pattern sharpness between the two detectors. Secondly, the whole SPED dataset was exported as a block (.blo) file and indexed using NanoMEGAS ASTAR software by the method of (Rauch, et al., 2010) and the results from each detector were compared.

RESULTS

The difference between the two detectors for SPED is obvious, as shown in Figure 1. The fluorescent screen camera shows significant noise, which manifests as a significant grey level between the spots. On the other hand, the direct detection camera gives much darker backgrounds between the spots. This is well illustrated by the line trace of intensity taken from top left to bottom right indicated by the arrow in both alpha patterns (taken from the same place in the sample). There is clearly real intensity between the spots visible in the data taken with the direct detection camera, as one would expect, since there will always be diffuse inelastic scattering in such patterns. But, this declines in an almost linear way on the logarithmic scaled plot towards the pattern edges. On the other hand, the data from the conventional camera plateaus towards the edges, indicating that this level is dominated by noise in the camera system. All of this makes weaker spots far easier to see with the direct detector.

Additionally, in the patterns from the beta area, there are clearly resolved split spots in the pattern on the direct detector. This probably indicates more than one phase in the area sampled by the beam, possibly a fine alpha lath as well as the beta. But this level of detail is just not present in the data from the conventional camera, there are blurred indications of spot splitting, but it is nowhere near as clear. This indicates that the Modulation Transfer Function on the Medipix camera is also far superior to that on the fluorescent screen / video camera combination. This would also make accuracy of any measurements based on peak position determination (e.g. strain analysis) much better.
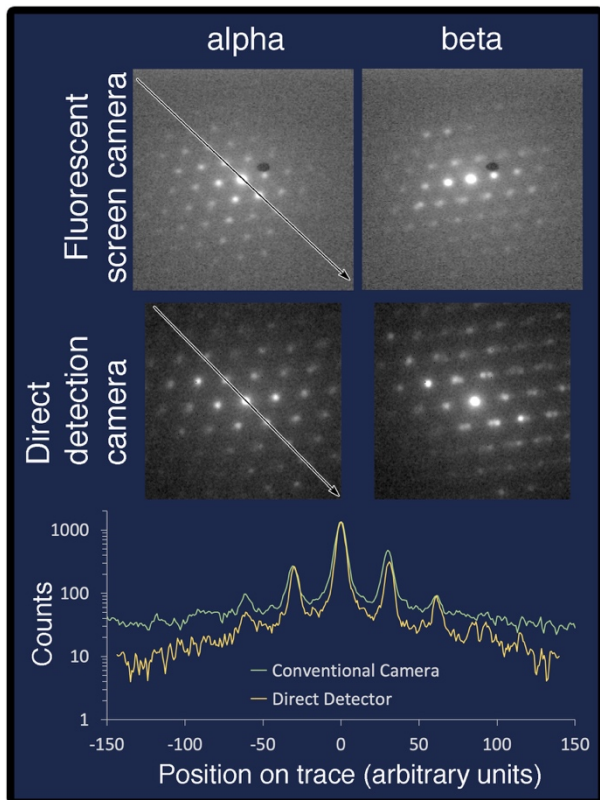
Figure 1: A comparison of precession electron diffraction patterns from alpha and beta titanium phases with the two cameras recorded under the same conditions (apart from an adjustment of camera length to cope with the different physical positions of the two cameras in the microscope column). The two pairs of diffraction patterns were single frames in the full datasets as shown in Figure 2 (red spots for alpha, cyan for beta). The black level in both images is set at zero counts. The white level is at the brightest point of the central spot. The graph shows a direct comparison of a trace across the alpha diffraction pattern. The counts for the direct detection camera are raw counts and should be close to the number of real electron hits in each pixel. The counts for the fluorescent screen camera are scaled to this.

Figure 2 shows maps made from almost identical areas of the same sample using the two cameras under the same conditions of beam current, convergence, precession angle, and pixel dwell time. The first images show virtual bright field images of the two, that is images of all electrons in the diffraction pattern falling inside an aperture defined in software to include the direct beam and no diffracted beams (Moeck, et al., 2011). Pure alpha areas, whether the large primary alpha grain to the lower right, or the larger secondary alpha laths are bright as these are primarily titanium and aluminium in content. The areas between the secondary alpha laths are beta titanium, rich in vanadium, and small tertiary alpha laths. The combination of the larger average atomic number and the density of boundaries means more scattering and a darker contrast than the low defect density, light alpha. Two dots are placed on each, the red one indicating the approximate location for the alpha diffraction pattern of Figure 1, and the cyan one indicating the approximate location for the beta diffraction pattern of Figure 1. It may also be noticed that the data from the direct detector is clearer and sharper, and this probably happens because of the lower noise level in the diffraction patterns resulting in sharper distinction between regions with different diffracted intensities.

The second pair of images shows the phase maps determined from this dataset, showing areas identified as alpha in red, and those identified as beta as cyan. While both maps show the same principal features and clearly find alpha and beta titanium in the expected locations, the conventional camera data misses many of the finest laths of alpha,

although the primary alpha grains and the large secondary alpha laths are found. This probably happens because the weak extra spots seen for alpha (e.g. 0001 reflections, which have no counterpart in beta) are not reliably detected for small laths in the presence of detector noise. It should be pointed out that despite the possibility for some distortion using the imaging of the phosphor screen on a retractable CCD camera for the conventional Stingray system, no evidence was seen of any distortion affecting indexing, as evidenced by the fact that large, single-phase regions are well indexed by this camera, and the regions with the biggest problems are those where there are fine laths.

This conclusion is clearly borne out by the third pair of images, which are phase reliability maps (a goodness of fit metric defined by the ASTAR software on how certain the fit to that phase is (Moeck, et al., 2011)). The phase reliability clearly goes rather low in the fine tertiary alpha areas in the conventional camera data, whereas there are lighter areas on the fine tertiary alpha areas in the direct detector data indicating better identification of the fine alpha, even in small diffracting volumes. The darkest areas (those with lowest phase reliability) appear to be interfaces, mainly between alpha laths and beta matrix, and these are probably characterised by overlapping patterns that are difficult to index uniquely. Quite why the beta is consistently darker on this map is a question for future work in applying precession electron diffraction to such alloys. It may be that the lattice parameter differs a little from the reference value used in calculating the pattern bank and that a small modification of this lattice parameter and recalculation of the pattern bank could yield improved results.

The fourth pair of images shows the crystallographic orientation of the z-direction (i.e. out of the page) in these maps on a colour scale. The purpose of the present paper is not to discuss the orientation data itself in great detail. Nevertheless, it is clear that the same results are found for the primary alpha, the beta, and the larger secondary alpha laths. What is missed in the data from the conventional camera is that the fine tertiary alpha is not always resolved, so there is little data on the multiplicity of orientations in those fine regions. At a first look there are at least 3 orientations in some of these areas, and there could be more. There are two reasons for this. Firstly, these maps were taken at a relatively coarse step size of ~15nm per pixel, so some fine details could have been missed). Secondly, there are 12 possible alpha orientations that can be produced by transformation from beta (Humbert, et al., 1995), and more careful analysis of the Euler angles for each lath would be needed to determine if it was the same crystal orientation as another one of similar color in the map.

Finally, the last pair of images shows the "orientation reliability" (a goodness of fit metric defined by the ASTAR software to quantify the degree of certainty in orientation measurement), on a simple black-white scale, where black is 0% and white is 100%. A far larger fraction of the image has high reliability using the direct detection camera, again showing that this is going to give much more trustworthy results, especially in complex nanostructured materials.
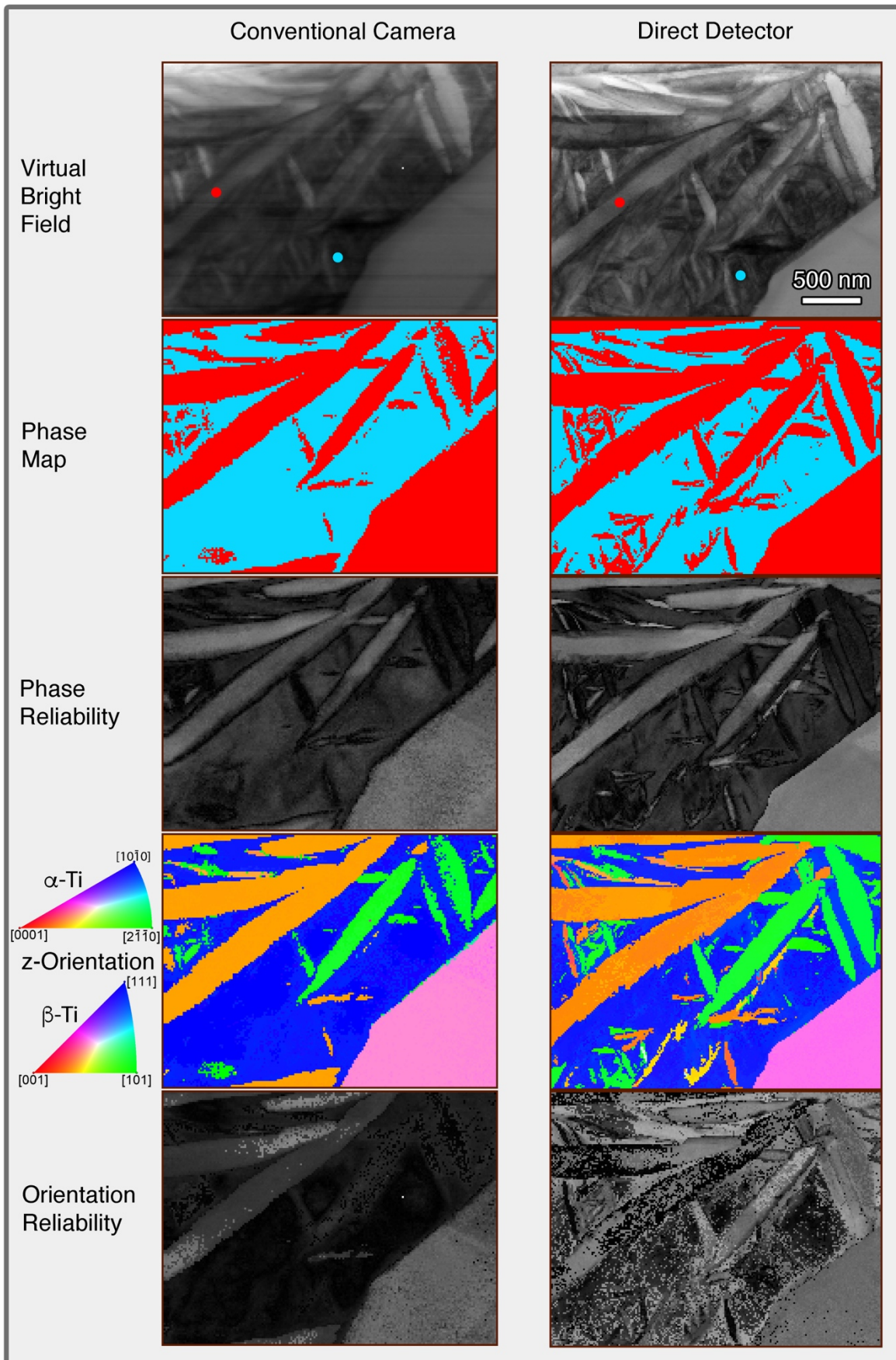
Figure 2: Orientation maps from SPED using the two detectors on approximately the same area. Showing a virtual bright field image, a phase map (red = alpha-Ti, cyan = beta-Ti), a phase reliability map (where white = 100%), a z-orientation map, and an orientation reliability map (where white = 100%).

To put all of this on a more quantitative footing, the two reliability index images were converted to histograms of all pixel values in each image and are shown in Figure 3. For the phase reliability, the two traces are rather similar at the low end, and it is just at the upper end that they diverge significantly. The means of the two distributions are 20.9 for the conventional camera and 23.0 for the direct detection camera. From this, we can conclude that in this case, the determination of the phase was mostly clear and unambiguous with both cameras, and even worked well at higher image noise levels. That said, there may be some failures hidden within these numbers for the CCD camera, as it was already established that the alpha was systematically under-reported for fine laths and some regions of alpha were reported as beta. This can happen as certain crystal directions show very similar diffraction patterns for the two phases, just with additional weak reflections for alpha. These may be too weak to strongly affect indexing in the case of a noisy diffraction pattern from a small diffracting volume, which could explain this effect.

On the other hand, the orientation reliability metric shows rather different histograms for the two cameras, with the main bulk of the distribution and main peak much higher for the direct detection camera. This results in totally different means for the distributions of 15.2 for the conventional camera and 27.6 for the direction detection camera. Which means that the lower noise in the direct detection data really gives a major advantage in improving the certainty of the orientation determination.
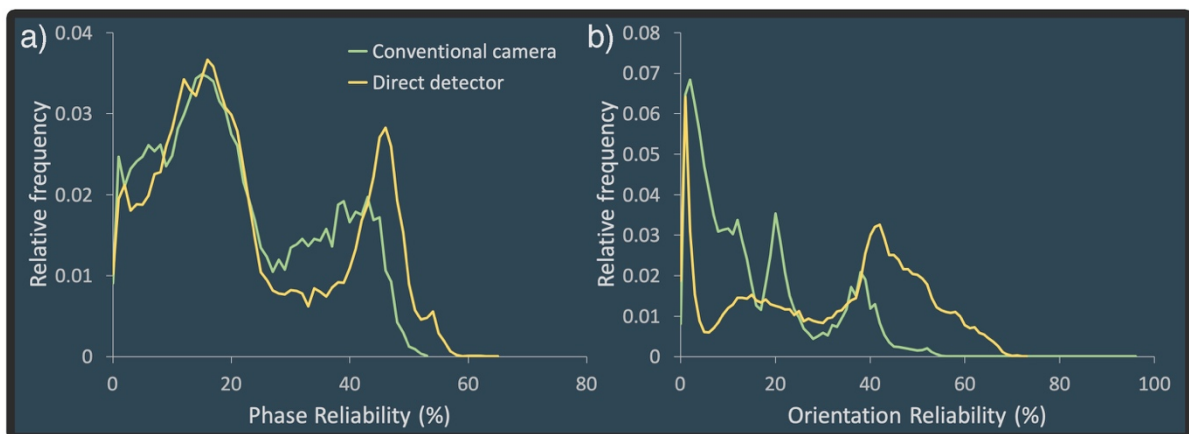

Figure 3: Reliability histogram plots for the indexing of Figure 2: a) phase reliability; b) orientation reliability

DISCUSSION

A first point on the suitability of this Merlin for EM detector (or similar small pixelated direct electron detectors) for scanning precession electron diffraction orientation mapping concerns the number of pixels required for mapping. It has already been well demonstrated in the literature that scanning precession electron diffraction works well with the small pixel numbers available on the conventional Stingray camera (maximum of 580x580, but usually 288x288 or 144x144) (Eggeman, et al., 2015; Estradé, et al., 2012; Martineau, et al., 2019; Rauch, et al., 2010; Rouvimov, et al., 2009). The reason is simple, as long as the spots are well separated, and shifts of spot positions between different phases or orientations are easily seen, then the main thing that is needed is high speed recording of intensity, and large reciprocal space resolution is not that important. Even in the case of strain measurement by precession electron diffraction, where small movements of diffraction spots would be more accurately measured with a larger number of pixels, it is found that the Stingray camera works well (Darbal, et al., 2014; Darbal, et al., 2013;

Reisinger, et al., 2016), or that 512x512 pixels on a different camera was excellent (Cooper, et al., 2017). Consequently, it can be concluded that the fact that the Merlin for EM detector only has 256x256 pixels is no obstacle whatsoever to its use for phase and orientation mapping, or indeed other applications of precession electron diffraction. Indeed, as stated in the introduction, detectors with such small pixel numbers and high speed readout are widely useful in a range of scanned diffraction applications, as was well summarized in the recent review by (Ophus, 2019).

Whilst some improvements could be made to a conventional precession system, principally by changing the phosphor on the small screen to reduce afterglow (which may also have affected the spatial resolution using the Stingray camera) and improving the optical coupling to the camera, resulting in better data quality, it is clear that the use of the electron counting detector provides a huge step forwards. Nevertheless, it is clear from detailed examination of Figure 2 that afterglow was not the limiting issue here, since this would reduce the resolution along the principal scan direction, which is the horizontal in these maps. The result would be that laths with a horizontal orientation would be better mapped than those with a more vertical orientation. Such an effect is not seen and in fact, several horizontal laths seen in the Merlin for EM data are invisible in the Stingray data, suggesting that the problem is more of identifying specifically characteristic extra spots for alpha in the noisy diffraction patterns than persistence of diffraction patterns from one scan point to the next due to afterglow on the phosphor.

Whilst the issues with pattern overlap and spot splitting were not addressed in this work, it is noted that recent matching strategies may well perform well in this area (Martineau, et al., 2019; Valery, et al., 2017) and that the improved data quality (especially lateral definition in the patterns) may actually give significant advantages in such cases.

All of this was performed with what was a small beam current for the microscope – an estimate from the counts recorded on the Merlin for EM counting detector suggested a value > 6.5pA. Moreover, it is clear that the beam current could be reduced further, although this was already the smallest possible spot size, smallest possible condenser aperture, and relatively short pixel acquisition time. Spread over a 15nm pixel at this beam current, this corresponds to ~19e$^-$Å^{-2}, which is approaching the levels required for cryo-electron microscopy or electron microscopy of a wide range of beam sensitive materials including biomedical samples of cell sections, and crystalline pharmaceuticals. It would be possible to increase acquisition rate to 200 patterns per second using 200Hz precession frequency, but this is the maximum precession frequency for the beam shift and tilt coils in this microscope, so we could probably halve the dose by making this change. It would only be possible to reduce the dose further by reducing the extraction voltage on the electron gun. Seeing as the current could be reduced, and the beam spread more, it may well be possible to perform useable crystal orientation mapping in unfixed biological and medical samples, and this may be of interest in studies of crystalline proteins, crystallised pharmaceuticals, and biomineralization.

It may also be that the pattern matching algorithm could be optimized to better make use of the low noise performance of a counting detector. Specifically, the quality index defined by (Rauch, et al., 2010) is just a normalized linear function of the intensities in the pattern and the calculated diffraction pattern. This means in practice that weak spots in both pattern and template are suppressed in the pattern matching, whether that is because they occur at higher angles or because they appear as superlattice spots with low structure factors. Thus, a spot of half the integrated intensity would contribute a quarter of the

weight, and one of a tenth of the integrated intensity would contribute 1% of the weight of a bright spot. A redesign of the quality index in the algorithm could improve the use of all spots in a pattern, for instance by applying a logarithmic intensity mapping to the patterns before cross correlation to reduce dynamic range, or normalizing the whole pattern by some smooth varying function which decays as a function of radius, prior to inclusion in the pattern matching algorithm. If something like the cross-correlation with a Gaussian (as done by (Hart, et al., 2016) or other suitable spot shape were performed (e.g. discs (Krajnak, et al., 2016)) prior to template matching, further exclusion of noise and diffuse scattering could be performed, thus giving even clearer detection of low intensity spots, including in data taken at low electron doses.

Additionally, processing the crystallographic data using the pattern matching algorithm of (Rauch, et al., 2010) is not the only possible method for analyzing data from polycrystalline or multiphase materials. Van Helvoort and colleagues have shown that other methods in machine learning / applied mathematics can be useful in classifying a dataset into a small number of significant components and thereby mapping phases in nanostructured materials (Martineau, et al., 2019; Sunde, et al., 2019; Sunde, et al., 2018). Such techniques are known to work well even with noisy data, so it is highly likely that the improved data quality from the direct electron detector will allow the successful application of such methods of very low electron doses of a few e$^-$Å^{-2}, just as was recently performed using scanned electron nanodiffraction for a beam-sensitive halide perovskite (Doherty, et al., 2020). Further data analysis could be performed in some cases using different approaches, by integrating the intensity of specific parts of a diffraction pattern (possibly with background subtraction) as has been done in other analyses of pixelated detector data from STEM (Nord, et al., 2019a; Nord, et al., 2019b; Paterson, et al., 2020). This could be done, for example, to study the ordering or domain variant selection in materials, by the appearance and orientation of superlattice spots. Another area where the low noise performance of this system would be extremely valuable would be in improving the sensitivity of strain measurement by precession electron diffraction, and this would be worth testing in future work.

CONCLUSIONS

We have demonstrated the successful integration of a direct electron counting detector into a scanned precession electron diffraction system. This has been tested by performing a scan of the same area in a two-phase titanium alloy with this new detector, and with the same system using a conventional video-camera-based detection system. It is found that the noise floor is significantly lower with the new detector, especially at higher diffracted angles where diffuse scattering is minimized. The results for orientation mapping mean that the phase identification and orientation determination is more reliable, fine features in the nanostructure are much more easily distinguished, and this happens because the weak signals from small diffracting regions pop up above the noise more easily. Seeing as this work was performed with just a few electrons per square Ångström and indexing was still reliable, it is suggested that precession electron diffraction using this detector would allow the collection of useful and interpretable spatially-resolved diffraction data on damage-sensitive materials such as biological thin sections, pharmaceuticals and proteins.

ACKNOWLEDGEMENTS

REFERENCES

BEACHAM, R., MAC RAIGHNE, A., MANEUSKI, D., O'SHEA, V., MCVITIE, S. & MCGROUTHER, D. (2011). Medipix2/Timepix detector for time resolved Transmission Electron Microscopy. J. Instrum. **6**, C12052.

COOPER, D., BERNIER, N., ROUVIÈRE, J.-L., WANG, Y.-Y., WENG, W., MADAN, A., MOCHIZUKI, S. & JAGANNATHAN, H. (2017). High-precision deformation mapping in finFET transistors with two nanometre spatial resolution by precession electron diffraction. Appl. Phys. Lett. **110**(22), 223109.

DARBAL, A.D., NARAYAN, R.D., VARTULI, C., AOKI, T., MARDINLY, J., NICOLOPOULOS, S. & WEISS, J.K. (2014). Applications of Automated High Resolution Strain Mapping in TEM on the Study of Strain Distribution in MOSFETs. Microsc. Microanal. **20**(S3), 1066-1067.

DARBAL, A.D., NARAYAN, R.D., VARTULI, C., LIAN, G., GRAHAM, R., SHAAPUR, F., NICOLOPOULOS, S. & WEISS, J.K. (2013). Automated High Precision Strain Measurement Using Nanobeam Diffraction Coupled with Precession. Microsc. Microanal. **19**(S2), 702-703.

DOHERTY, T.A.S., WINCHESTER, A.J., MACPHERSON, S., JOHNSTONE, D.N., PAREEK, V., TENNYSON, E.M., KOSAR, S., KOSASIH, F.U., ANAYA, M., ABDI-JALEBI, M., ANDAJI-GARMAROUDI, Z., WONG, E.L., MADÉO, J., CHIANG, Y.-H., PARK, J.-S., JUNG, Y.-K., PETOUKHOFF, C.E., DIVITINI, G., MAN, M.K.L., DUCATI, C., WALSH, A., MIDGLEY, P.A., DANI, K.M. & STRANKS, S.D. (2020). Performance-limiting nanoscale trap clusters at grain junctions in halide perovskites. Nature **580**(7803), 360-366.

EGGEMAN, A.S., KRAKOW, R. & MIDGLEY, P.A. (2015). Scanning precession electron tomography for three-dimensional nanoscale orientation imaging and crystallographic analysis. Nat Commun **6**, 7267.

ESTRADÉ, S., PORTILLO, J., MENDOZA, J., KOSTA, I., SERRET, M., MÜLLER, C. & PEIRÓ, F. (2012). Assessment of misorientation in metallic and semiconducting nanowires using precession electron diffraction. Micron **43**(8), 910-915.

GJØNNES, J., HANSEN, V., BERG, B.S., RUNDE, P., CHENG, Y.F., GJØNNES, K., DORSET, D.L. & GILMORE, C.J. (1998). Structure model for the phase AlmFe derived from three-dimensional electron diffraction intensity data collected by a precession technique. Comparison with convergent-beam diffraction. Acta Crystallogr A **54**, 306-319.

GJØNNES, K. (1997). On the integration of electron diffraction intensities in the Vincent-Midgley precession technique. Ultramicroscopy **69**(1), 1-11.

HART, M.J., BASSIRI, R., BORISENKO, K.B., VERON, M., RAUCH, E.F., MARTIN, L.W., ROWAN, S., FEJER, M.M. & MACLAREN, I. (2016). Medium range structural order in amorphous tantala spatially resolved with changes to atomic structure by thermal annealing. J. Non-Cryst. Solids **438**, 10-17.

HUMBERT, M., WAGNER, F., MOUSTAHFID, H. & ESLING, C. (1995). Determination of the Orientation of a Parent [beta] Grain from the Orientations of the Inherited [alpha] Plates in the Phase Transformation from Body-Centred Cubic to Hexagonal Close Packed. J Appl Crystallogr **28**(5), 571-576.

JOHNSTONE, D.N., CROUT, P., LAULAINEN, J., HØGÅS, S., MARTINEAU, B., BERGH, T., SMEETS, S., FRANCIS, C., OPHEIM, E., PRESTAT, E., COLLINS, S., DANAIE, M., FURNIVAL, T., ÅNES, H.W., MORZY, J., IQBAL, A., DOHERTY, T., VON LANY, M., OSTASEVICIUS, T., TOVEY, R., JACOBSEN, E. & POON, T. (2020a). pyxem/pyxem: pyxem 0.11.0, https://doi.org/10.5281/zenodo.3831473.

JOHNSTONE, D.N., FIRTH, F.C.N., GREY, C.P., MIDGLEY, P.A., CLIFFE, M.J. & COLLINS, S.M. (2020b). Direct Imaging of Correlated Defect Nanodomains in a Metal–Organic Framework. J Am Chem Soc **142**(30), 13081-13089.

KOLB, U., GORELIK, T., KÜBEL, C., OTTEN, M.T. & HUBERT, D. (2007). Towards automated diffraction tomography: Part I—Data acquisition. Ultramicroscopy **107**(6), 507-513.

KRAJNAK, M., MCGROUTHER, D., MANEUSKI, D., O'SHEA, V. & MCVITIE, S. (2016). Pixelated detectors and improved efficiency for magnetic imaging in STEM differential phase contrast. Ultramicroscopy **165**, 42-50.

MAC RAIGHNE, A., FERNANDEZ, G.V., MANEUSKI, D., MCGROUTHER, D. & O'SHEA, V. (2011). Medipix2 as a highly flexible scanning/imaging detector for transmission electron microscopy. J. Instrum. **6**, C01047.

MARTINEAU, B., JOHNSTONE, D.N., VAN HELVOORT, A.T.J., MIDGLEY, P.A. & EGGEMAN, A.S. (2019). Unsupervised machine learning applied to scanning precession electron diffraction data. Advanced Structural and Chemical Imaging **5**, 3.

MIR, J.A., CLOUGH, R., MACINNES, R., GOUGH, C., PLACKETT, R., SHIPSEY, I., SAWADA, H., MACLAREN, I., BALLABRIGA, R., MANEUSKI, D., O'SHEA, V., MCGROUTHER, D. & KIRKLAND, A.I. (2017). Characterisation of the Medipix3 detector for 60 and 80 keV electrons. Ultramicroscopy **182**, 44-53.

MOECK, P., ROUVIMOV, S., RAUCH, E.F., VÉRON, M., KIRMSE, H., HÄUSLER, I., NEUMANN, W., BULTREYS, D., MANIETTE, Y. & NICOLOPOULOS, S. (2011). High spatial resolution semi-automatic crystallite orientation and phase mapping of nanocrystals in transmission electron microscopes. Crystal Research and Technology **46**(6), 589-606.

MUGNAIOLI, E., GORELIK, T. & KOLB, U. (2009). "Ab initio" structure solution from electron diffraction data obtained by a combination of automated diffraction tomography and precession technique. Ultramicroscopy **109**(6), 758-765.

NORD, M., ROSS, A., MCGROUTHER, D., BARTHEL, J., MOREAU, M., HALLSTEINSEN, I., TYBELL, T. & MACLAREN, I. (2019a). Three-dimensional subnanoscale imaging of unit cell doubling due to octahedral tilting and cation modulation in strained perovskite thin films. Physical Review Materials **3**(6), 063605.

NORD, M., SEMISALOVA, A., KÁKAY, A., HLAWACEK, G., MACLAREN, I., LIERSCH, V., VOLKOV, O.M., MAKAROV, D., PATERSON, G.W., POTZGER, K., LINDNER, J., FASSBENDER, J., MCGROUTHER, D. & BALI, R. (2019b). Strain Anisotropy and Magnetic Domains in Embedded Nanomagnets. Small **15**(52), 1904738.

OPHUS, C. (2019). Four-Dimensional Scanning Transmission Electron Microscopy (4D-STEM): From Scanning Nanodiffraction to Ptychography and Beyond. Microsc. Microanal. **25**(3), 563-582.

PATERSON, G.W., WEBSTER, R.W.H., ROSS, A., PATON, K.A., MACGREGOR, T.A., MCGROUTHER, D., MACLAREN, I. & NORD, M. (2020). Fast Pixelated Detectors in Scanning Transmission

Electron Microscopy. Part II: Post Acquisition Data Processing, Visualisation, and Structural Characterisation. In *arXiv e-prints*, pp. arXiv:2004.02777.

PENNYCOOK, T.J., LUPINI, A.R., YANG, H., MURFITT, M.F., JONES, L. & NELLIST, P.D. (2015). Efficient phase contrast imaging in STEM using a pixelated detector. Part 1: Experimental demonstration at atomic resolution. Ultramicroscopy **151**, 160-167.

RAMACHANDRA, R., BOUWER, J.C., MACKEY, M.R., BUSHONG, E., PELTIER, S.T., XUONG, N.H. & ELLISMAN, M.H. (2014). Improving Signal to Noise in Labeled Biological Specimens Using Energy-Filtered TEM of Sections with a Drift Correction Strategy and a Direct Detection Device. Microsc. Microanal. **20**(3), 706-714.

RAUCH, E.F., PORTILLO, J., NICOLOPOULOS, S., BULTREYS, D., ROUVIMOV, S. & MOECK, P. (2010). Automated nanocrystal orientation and phase mapping in the transmission electron microscope on the basis of precession electron diffraction. Z. Krist.-Cryst. Mater. **225**(2-3), 103-109.

REISINGER, M., ZALESAK, J., DANIEL, R., TOMBERGER, M., WEISS, J.K., DARBAL, A.D., PETRENEC, M., ZECHNER, J., DAUMILLER, I., ECKER, W., SARTORY, B. & KECKES, J. (2016). Cross-sectional stress distribution in AlxGa1-xN heterostructure on Si(111) substrate characterized by ion beam layer removal method and precession electron diffraction. Materials & Design **106**, 476-481.

ROUVIMOV, S., RAUCH, E.F., MOECK, P. & NICOLOPOULOS, S. (2009). Automated Crystal Orientation and Phase Mapping of Iron Oxide Nano-Crystals in a Transmission Electron Microscope. Microsc. Microanal. **15**(S2), 1290-1291.

RUSKIN, R.S., YU, Z.H. & GRIGORIEFF, N. (2013). Quantitative characterization of electron detectors for transmission electron microscopy. J. Struct. Biol. **184**(3), 385-393.

RYLL, H., SIMSON, M., HARTMANN, R., HOLL, P., HUTH, M., IHLE, S., KONDO, Y., KOTULA, P., LIEBEL, A., MULLER-CASPARY, K., ROSENAUER, A., SAGAWA, R., SCHMIDT, J., SOLTAU, H. & STRUDER, L. (2016). A pnCCD-based, fast direct single electron imaging camera for TEM and STEM. J. Instrum. **11**, 19, P04006.

SUNDE, J.K., JOHNSTONE, D.N., WENNER, S., VAN HELVOORT, A.T.J., MIDGLEY, P.A. & HOLMESTAD, R. (2019). Crystallographic relationships of T-/S-phase aggregates in an Al-Cu-Mg-Ag alloy. Acta Mater. **166**, 587-596.

SUNDE, J.K., MARIOARA, C.D., VAN HELVOORT, A.T.J. & HOLMESTAD, R. (2018). The evolution of precipitate crystal structures in an Al-Mg-Si(-Cu) alloy studied by a combined HAADF-STEM and SPED approach. Mater. Charact. **142**, 458-469.

TATE, M.W., PUROHIT, P., CHAMBERLAIN, D., NGUYEN, K.X., HOVDEN, R., CHANG, C.S., DEB, P., TURGUT, E., HERON, J.T., SCHLOM, D.G., RALPH, D.C., FUCHS, G.D., SHANKS, K.S., PHILIPP, H.T., MULLER, D.A. & GRUNER, S.M. (2016). High Dynamic Range Pixel Array Detector for Scanning Transmission Electron Microscopy. Microsc. Microanal. **22**(1), 237-249.

VALERY, A., RAUCH, E.F., CLÉMENT, L. & LORUT, F. (2017). Retrieving overlapping crystals information from TEM nano-beam electron diffraction patterns. J Microsc-Oxford **268**(2), 208-218.

VINCENT, R. & MIDGLEY, P.A. (1994). Double conical beam-rocking system for measurement of integrated electron diffraction intensities. Ultramicroscopy **53**(3), 271-282.

YANG, H., JONES, L., RYLL, H., SIMSON, M., SOLTAU, H., KONDO, Y., SAGAWA, R., BANBA, H., MACLAREN, I. & NELLIST, P.D. (2015a). 4D STEM: High efficiency phase contrast imaging using a fast pixelated detector. J Phys Conf Ser **644**, 012032, 012032.

YANG, H., MACLAREN, I., JONES, L., MARTINEZ, G.T., SIMSON, M., HUTH, M., RYLL, H., SOLTAU, H., SAGAWA, R., KONDO, Y., OPHUS, C., ERCIUS, P., JIN, L., KOVACS, A. & NELLIST, P.D. (2017).

Electron ptychographic phase imaging of light elements in crystalline materials using Wigner distribution deconvolution. Ultramicroscopy **180**, 173-179.

YANG, H., PENNYCOOK, T.J. & NELLIST, P.D. (2015b). Efficient phase contrast imaging in STEM using a pixelated detector. Part II: Optimisation of imaging conditions. Ultramicroscopy **151**, 232-239.